Renewable Energy 228 (2024) 120662

Contents lists available at ScienceDirect

Renewable Energy

journal homepage: www.elsevier.com/locate/renene

Neural network survivability approach of a wave energy converter considering uncertainties in the prediction of future knowledge ☆

Zahra Shahroozi [a,*], Malin Göteman [a,b], Jens Engström [a]

[a] Department of Electrical Engineering, Uppsala University, Ångströmlaboratoriet, Lägerhyddsvägen 1, Uppsala, 752 37, Sweden
[b] Centre of Natural Hazards and Disaster Science (CNDS), Villavägen 16, Uppsala, 752 36, Sweden

ARTICLE INFO

Keywords:
Wave energy converters
Survivability
Neural networks
Prediction of system dynamics
Extreme sea state
Wave tank experiment

ABSTRACT

To tune the wave energy converter (WEC) controller parameters such as damping to reduce the line force during extreme wave conditions, future knowledge of the line force is required. To achieve this, the incoming wave and system state should be predicted for a few seconds in the future. It is rather an arduous task to predict the future knowledge of waves and the system's dynamic when dealing with breaking and steep waves, and the system is subject to various nonlinear forces. The classical model-based control strategies often rely on linear assumptions to estimate the WEC dynamics for the sake of simplicity. Unlike the model-based, the data-driven approaches are free from modeling errors and the algorithms are trained over the true and noisy data to predict non-linear system behaviors. Using data-driven approaches, we are able to model nonlinear dynamics. However, new questions emerge on the accuracy of the future wave and system state predictions, and how this uncertainty propagates into the final prediction of the line force. As incorrect damping may lead to excessive line force and detrimental damage to the system, these are the knowledge gaps that need to be addressed. The main purpose of this paper is to answer these questions through a survivability strategy for wave energy converters by providing a realistic perspective on the implementation of the neural network approaches by accounting for the errors in the input data. For this purpose, a series of neural networks is designed that first predicts the surface elevation for 0.36 s ahead, i.e. corresponding to 2 s in the full-scale WEC. This future knowledge of the wave elevation is then used to predict the system state (i.e. power take-off (PTO) translator position) for the same prediction horizon based on the PTO damping. This information is then fed to a convolutional neural network (CNN) that predicts the peak line force 0.36 s ahead. This paper also evaluates the predictive capabilities of neural network (NN) models, comparing them to classical autoregressive (AR) and Kalman filter methods. While the AR model exhibits slightly higher accuracy in fixed PTO system configurations, it falters in providing real-time predictions when system parameters undergo variations. In contrast, the NN prediction model excels by establishing a robust relationship between system configuration and output signals. Especially noteworthy is its ability to outperform classical methods with minimal training on a selective set of system configurations. Then, the sensitivity of the peak line force prediction to the uncertainties in the input data from NN models and the prediction horizon is analyzed. The neural network models are trained over the experimental data subjected to extreme sea states for a point absorber wave energy converter. The results suggest that the accuracy of the surface elevation prediction has an insignificant direct effect on the peak force prediction model. However, these uncertainties are reflected in the PTO translator position prediction, and the model is considerably sensitive to the accuracy of this prediction. This sensitivity nonetheless is less notable for higher PTO damping values.

1. Introduction

In order for wave energy converters (WECs) to withstand challenging extreme wave conditions, it is essential to avoid forces exceeding design thresholds, aiming to prevent over-design of the structure and subsequently reduce their Levelized Cost of Energy (LCOE). Survival strategies may involve tuning system parameters (e.g., damping) or adopting avoidance measures (e.g., submergence) [1]. These strategies

☆ This research is supported by the Swedish Energy Agency, Sweden (project number 47264-1), the Swedish Research Council (grant number 2020-03634), and StandUp for Energy.
* Corresponding author.
E-mail address: zahra.shahroozi@angstrom.uu.se (Z. Shahroozi).

https://doi.org/10.1016/j.renene.2024.120662
Received 10 March 2023; Received in revised form 2 May 2024; Accepted 13 May 2024
Available online 15 May 2024

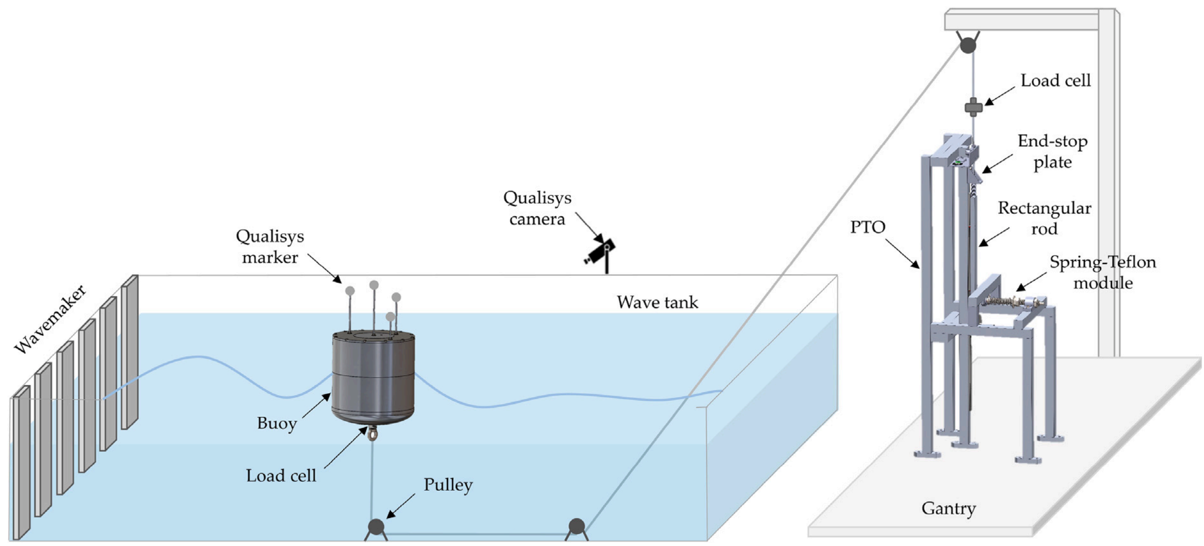

Fig. 1. Wave tank experimental setup schematic.
Source: Retrieved from [2]

rely on a profound understanding of the system's dynamics and the establishment of an accurate control system for survivability.

Control strategies often depend on predicting future knowledge of incoming incident waves [3] and wave excitation forces [4–7]. Various prediction models, including autoregressive (AR) models [4,8–10], autoregressive moving average models (ARMA) [4,11,12], the Kautz method [12], Kalman filter (KF) methods [5,13–16], and Neural Networks [4,7], have been developed, each characterized by distinct performance features. For instance, a comparative assessment between AR and ARMA models suggests that the latter produces results similar to AR models but introduces a more complex solution [9]. In [3], surface elevation prediction was achieved using the nonlinear autoregressive with exogenous input network (NARX NN) with promising results. In [7], the wave excitation force was calculated using a nonlinear autoregressive (NAR) neural network, group method of data handling (GMDH) network, and Long Short-Term Memory (LSTM) network, with all methods providing satisfactory performance.

Several data-driven and model-based control schemes have been proposed, primarily focusing on power maximization for a WEC under operational wave conditions [17–23]. In [22], a model-based control scheme demonstrated close-to-optimum performance in irregular waves, dependent on the prediction quality of the wave force. Mostly, linear assumptions are used in model-based approaches to estimate WEC dynamics for simplicity, leading to significant uncertainty in controller performance under various nonlinear phenomena. Machine learning approaches [24], such as neural network models, offer an alternative solution, being free from modeling errors, and trained over true and noisy data to predict the next instance of the parameter of interest [20]. In [18,19], online model-free reinforcement learning (RL) algorithms were proposed as resistive and reactive control schemes, respectively, demonstrating accurate system parameter identification.

The main objective of this paper is to provide a realistic estimate of the total uncertainties involved in predicting surface elevation, system state, and peak line force subjected to extreme waves using the neural network (NN) approach. Additionally, the sensitivity of this NN approach to uncertainties in various input data parameters is quantified. Moreover, autoregressive (AR) and Kalman filter (KF) methods are investigated within the framework of a fixed system configuration. Nevertheless, their limitations become evident when extended to continuous control inputs, primarily due to their incapability to dynamically adjust to real-time variations in system parameters and establish a direct link between system input parameters and output. This underscores the necessity to explore alternative methodologies, with a specific emphasis on mapping the intricate dependency of the system output to the system parameters, such as PTO damping, in the dynamic context of wave energy applications.

The survivability strategy adopted here minimizes the line force by finding the optimal damping. NN models are trained using wave tank experimental data designed to study system dynamics under extreme sea states. The experimental data inherit nonlinear phenomena such as wave breaking [25], wave breaking slamming [26], and overtopping [27], providing an ideal dataset for this analysis. The novelties include: i) quantifying the sensitivity of peak force prediction to uncertainties in NN input data, ii) developing NN models to predict PTO translator position, surface elevation, and peak line force for a point absorber WEC subjected to extreme wave conditions, iii) comparing the estimated optimum damping for survivability, considering different accuracy levels of prediction in NN input data.

The remainder of the paper is as follows: the wave tank experiment and NN prediction, as well as AR and KF methods, are described in Section 2, Section 3, Section 4, and Section 5, respectively. The results and discussion are presented in Section 6. Lastly, the conclusions are drawn in Section 7.

2. Wave tank experiment

A wave tank experiment with a scale of 1:30 was conducted in the Ocean and Coastal Engineering Laboratory of Aalborg University, Denmark. The setup consisted of an aluminum cylindrical buoy with ellipsoidal bottom, and a friction-damping linear PTO system, i.e. rubbing against the spring-Teflon module by its vertical movement and applying a constant sliding friction force, see Fig. 1.

Different PTO damping configurations were considered including three constant PTO sliding friction damping forces of $F_{D_0} \approx 0$ N, $F_{D_1} \approx 7.4$ N, and $F_{D_2} \approx 18.9$ N, that are referred to as D_0, D_1, and D_2 damping cases in this paper, respectively. The fourth damping case was the infinite damping *coefficient* i.e. corresponding to a locked PTO, refer to [28,29]. The PTO was constrained only by an upper end-stop spring with a coefficient of 5.9 N/mm. In this study, to maintain the focus on the constant sliding friction damping forces, only damping cases D_0, D_1, and D_2 are considered.

The extreme sea states with a 50-year return period from an environmental contour for the Dowsing site in the North Sea were selected, see Fig. 2. The sea states were scaled 1:30 using the Froude-scaling law to be generated by the wavemaker in the wave tank. The time interval of 10 min, corresponding to about one hour for the full-scale model,

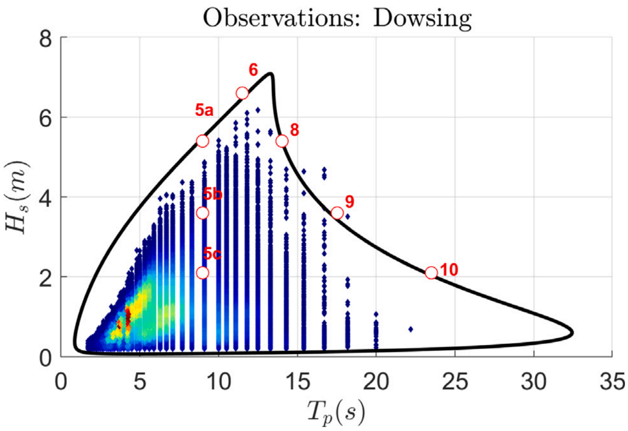

Fig. 2. The 50-year return period environmental contour constructed based on the I-Form hybrid method [30] for the Dowsing site in the North Sea is illustrated for a full-scale system. The seven circles represent the selected sea states for this experimental setup. The axes show the peak period (T_p) and significant wave height (H_s).
Source: Adapted from [31]

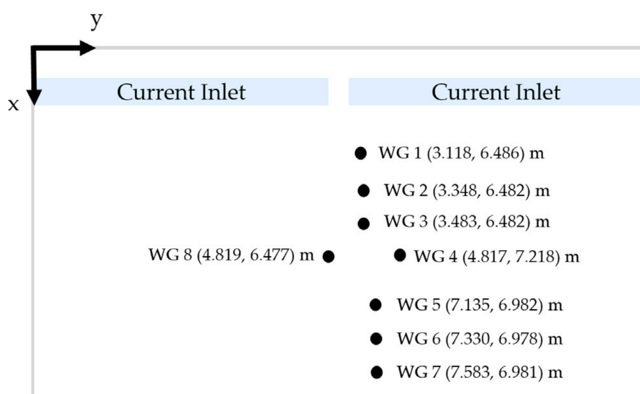

Fig. 3. The wave gauges position is shown where the buoy is located in the location of wave gauge 8 after wave calibration, and then, the wave gauge 8 is relocated to its closest vicinity in the direction of the y-axis.

was considered to generate the irregular waves, i.e. sea states 5a to 10, during the wave tank experiment. In this paper, the most extreme sea state, i.e. sea state 6, is analyzed which is identified with the most often nonlinear phenomena. Hence, it makes an excellent case for the purpose of studying the uncertainties within the prediction of future knowledge and peak line forces.

The measurement system was synchronized and comprised of: (i) four Qualisys cameras to track the buoy motion; (ii) a draw-wire position sensor to capture the PTO translator's vertical movement; (iii) two load cells to log the line force data: one installed at the buoy and the other at the PTO translator; iv) eight wave gauges to measure the surface elevation, see Fig. 3. The sampling frequency was 256 Hz except for the Qualisys which had a sampling frequency of 300 Hz. The experimental setup properties and sea state characteristics are summarized in Table 1. For further details about the experimental setup refer to [32], and [28].

The line force seen by the PTO from the buoy side is measured by a load cell and can be also derived from the equation of motion in vector form as:

$$m_{\text{PTO}}\ddot{\mathbf{z}} = \mathbf{F}_{\text{line}} + \mathbf{F}_{\text{endstop}} + \mathbf{F}_{f_{\text{PTO}}} + \mathbf{F}_{fp} + m_{\text{PTO}}\mathbf{g} \tag{1}$$

where m_{PTO} is the total PTO translator mass including all the equipment attached to it. Further, the end-stop spring, PTO, and pulley friction forces are $\mathbf{F}_{\text{endstop}}$, $\mathbf{F}_{f_{\text{PTO}}}$, and $\mathbf{F}_{fp}$, respectively. Moreover, $\ddot{\mathbf{z}}$ is the PTO

Table 1
Wave tank experiment setup and properties, adopted from [28]. Note that the coordinate system for the center of gravity reported for the buoy is located at the bottom center of the buoy, while its moments of inertia are computed based on a coordinate system located at the center of gravity with the z-axis in the upright vertical direction.

Description	Value	Unit
PTO		
Mass	2.138 ± 0.001	kg
Stroke length	220	mm
End-stop spring coefficient	5.9	N/mm
Buoy		
Mass	15.73 ± 0.001	kg
Diameter, height, draft	330 × 380 × 230	mm
Center of gravity (x_{CG}, y_{CG}, z_{CG})	0 × 0 × 118.6	mm
Moment of inertia (I_{xx}, I_{yy}, I_{zz})	0.3537 ×0.3536× 0.2918	kg m^2
Wave tank		
Dimension*	13 × 8 × 1.5	m
Buoy's position from wavemaker	4.819	m
Buoy's position from side walls	6.477, 6.54	m
Water depth	0.73 ± 0.02	m
Sensors		
Position sensor measurement range	1000 ± 0.3	mm
Load cell capacity	2000	N
Qualisys	4 cameras	–
Wave gauges	8 probes	–
Sea state characteristics for 1:30 scaled system		
Sea states	S5a, S5b, S5c, S6, S8, S9, S10	–
Significant wave height (H_s)	0.18, 0.12, 0.07, 0.22, 0.18, 0.12, 0.07	m
Peak period (T_p)	1.64, 1.64, 1.64, 2.10, 2.56, 3.20, 4.29	s

acceleration, and $\mathbf{g}$ is the gravitational acceleration. Note that the PTO friction force and the pulley friction force have a nonlinear nature in this equation.

2.1. Experimental surface elevation data

A short window of the time series, and the spectrum of the measured surface elevation at the buoy location for the sea state 6 with H_s = 0.22 m and T_p = 2.10 s, are shown in Fig. 4. Different damping configurations show insignificant variation in both the spectrum and time series. This implies that the surface elevation can be safely predicted independent of the WEC damping and yet provide the required information for the peak force prediction.

2.2. Experimental translator position data

Higher damping configurations limit the PTO translator's position amplitude, while lower damping cases lead to larger movement of the translator with more end-stop engagement. Fig. 5 shows that as the damping increases, a narrower distribution of the position is obtained as the distance between the first and third quartile decreases. Thus, the prediction of the PTO translator position is highly dependent on the damping configuration.

2.3. Experimental force data

The line force was affected by various nonlinear phenomena, the influence of which was more dominant in one damping configuration than the other. For instance, overtopping was more seen in higher damping cases where the movement of the WEC was constrained. On the other hand, frequent end-stop spring compression was experienced in the lower damping configurations where wave-breaking slamming was governing. These findings are thoroughly discussed and shown in [28].

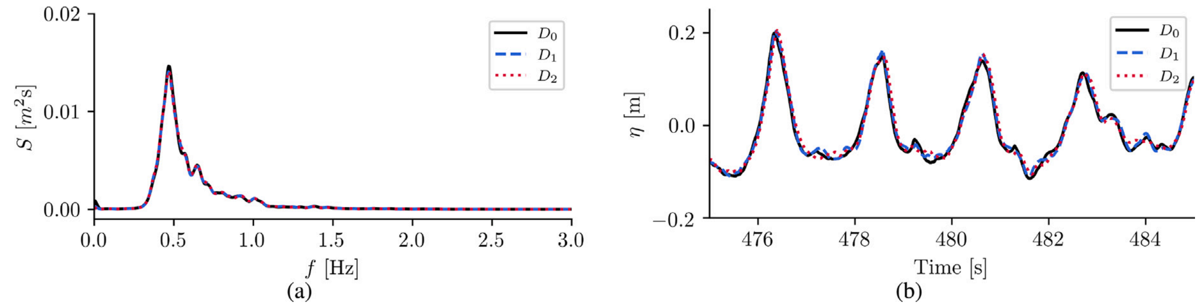

Fig. 4. The spectral density of the surface elevation and a few seconds of its time series are shown in (a) and (b), respectively, for the 1:30 scaled system.

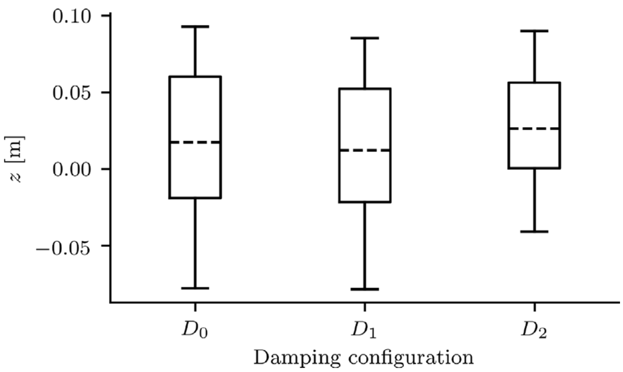

Fig. 5. The box plot of the PTO translator position data in different damping configurations. The box extends from the 25th (first quartile) to the 75th percentile (third quartile) of the data and the whiskers show the 5th and 95th percentiles. The dashed line shows the mean value. This figure is for the 1:30 scaled system.

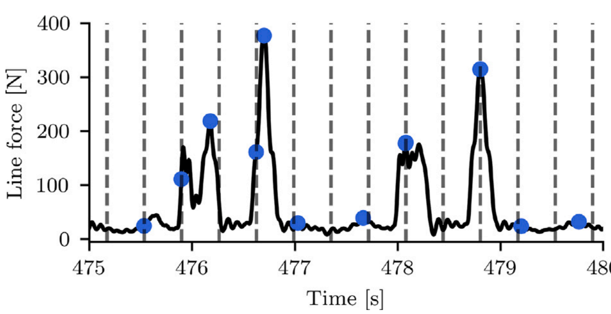

Fig. 6. The peak force for each block of 0.36 s, shown for a few seconds of the line force signal for the 1:30 scaled system.

The line force data is divided into non-overlapping blocks of equal length of 0.36 s. The peak force data contains the maximum values of each block, see Fig. 6

3. Neural network prediction models

3.1. Data-flow diagram

The flow of the data between the series of neural networks to predict the line force is shown in Fig. 7 which depicts where the past and future knowledge of surface elevation and PTO translator position enter the problem. Every 0.36 s (i.e. corresponding to 2 s in the full-scale WEC), the surface elevation, PTO translator position, and the peak line forces are computed for a range of damping and the damping value that gives the lowest peak force is identified as *the optimum damping* to fulfill the survivability purpose.

3.2. Normalization

The normalization, recognized as a critical pre-processing step that enhances convergence and overall performance, serves to standardize the magnitude of the data. This process ensures that the neural network operates within a consistent framework, contributing significantly to the overall improvement in system performance. The input and output data of the networks are normalized with a constant value corresponding to the maximum of each signal. Note that the maximum value of each signal is rounded up to its nearest integer value. Hence, the normalized line force is $F_{\mathrm{line}_n} = F_{\mathrm{line}}/400$, the surface elevations at WG8 and WG2 are normalized as $\eta_n = \eta/0.3$, and the PTO translator position and sliding damping forces are normalized as $z_n = z/0.2$ and $F_{D_n} = F_D/18.9$, respectively.

3.3. Generic setup

The prediction of surface elevation, PTO translator position, and peak line forces are achieved through neural network (NN) models implemented using the Keras library in Python [33,34]. These models are specifically structured as a deep neural network (DNN) for surface elevation and PTO translator position, along with a Convolutional Neural Network (CNN) for peak line force.

The hyperparameters for each NN model play a crucial role in determining their performance. To optimize these parameters, a thorough grid search is conducted. The grid search systematically explores a predefined range of hyperparameter values, such as learning rates, batch sizes, and layer configurations. For each combination of hyperparameters, the model is trained and evaluated, allowing for the identification of the most effective configuration. The chosen hyperparameter configurations, derived from this exhaustive grid search, are outlined in Table 2. This meticulous selection process ensures that the neural network models are finely tuned to provide accurate predictions.

Activation functions are essential in neural networks, adding nonlinearity to capture complex data relationships. Regularization methods, like L_2, counter overfitting by penalizing large weights through the addition of their squared sum to the loss function. Optimization methods such as Adam then tune network parameters during the training process, to minimize the loss function. For a comprehensive understanding of the neural network learning process and detailed information on hyperparameters, refer to [35].

All models predict signals 0.36 s into the future, equivalent to a 2-second forecast in the full-scale system. The datasets are uniformly divided across all networks into three subsets: 70% for the training set, 10% for validation, and the remaining 20% for testing.

The network training has been performed via a standard laptop computer, featuring AMD Ryzen 7 PRO 4750U processor at 1.70 GHz and 32 GB memory, taking a few minutes to less than an hour for all the NN models except for the PTO translator position model using one CPU core. The NN model for the PTO translator position has been trained via the Uppsala Multidisciplinary Center for Advanced Computational Science (UPPMAX) cluster using 2 nodes each consisting

Table 2
The table provides details on the hyperparameters utilized in the predictive neural network models. The initial learning rate for the Adam optimizer is set at 0.0001 and undergoes a gradual decrease by a factor of 0.67 in the event of insufficient improvement after ten epochs, eventually reaching a minimum value of 0.00001.

Hyperparameter	Surface elevation DNN	PTO translator position DNN	Peak line force CNN
Number of hidden layers	8	8	4
Number of nodes	128	128	128
Activation function	Hyperbolic tangent	Hyperbolic tangent	PReLU
Regularization	L_2	L_2	L_2
Regularization rate	0.0001	0.0001	0.0001
Optimization method	Adam	Adam	Adam
Batch size	128	256	32

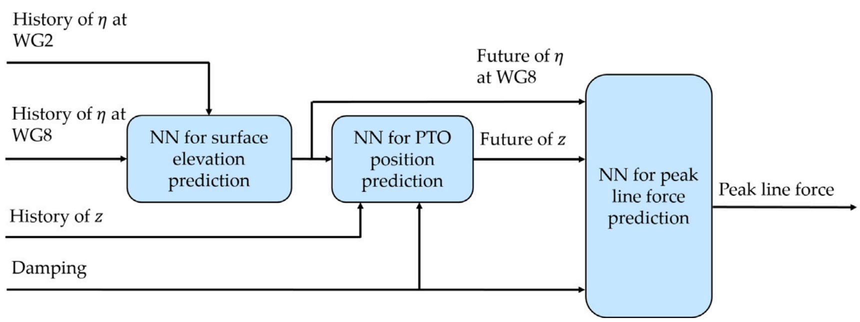

Fig. 7. The information flow in the computation of peak line forces.

of two Intel Xeon E5 2630 v4 at 2.20 GHz/core taking about two hours of computational time. Further information about the UPPMAX cluster can be found in [36].

3.4. Surface elevation DNN model architecture

The input to the DNN model is the history of surface elevation data: (i) at wave gauge 8, i.e. at the closest vicinity of the buoy, and (ii) at wave gauge 2, i.e. upstream of the buoy. The history signals from the two wave gauges are then concatenated and fed to the network. The output of the model predicts the surface elevation at the position of wave gauge 8. The higher and lower bound of the history required for this prediction is determined from the auto-correlation function of the surface elevation at wave gauge 8 as well as the correlation function between the signals from wave gauges 8 and 2. The signal is correlated with its delayed copy if the auto-correlation is above a certain threshold, and the corresponding time for this threshold is called the coherence time, [6,37], which marks the upper bound of the required history. Fig. 8 indicates the coherence time of around 15 s. On the other hand, the lower bound is around 0.7 s at which the correlation between the signal at wave gauge 2 and wave gauge 8 is maximum. For this model, a history of 2.7 s, corresponding to 702 data points, is used to predict the next 0.36 s. The total datasets contain all the possible windows of 0.36 s of the signal and include $150282 \times 70\% = 105197$ datasets for training, $150282 \times 10\% = 15028$ for validation, and $150282 \times 20\% = 30056$ for testing.

3.5. PTO translator position NN model architecture

The DNN architecture for the PTO translator position is characterized by a sequential network structure, incorporating both past information of the PTO translator position and future prediction of surface elevation and damping force as input. The required historical context of the PTO translator position is established at 2.7 s, equivalent to 15 s in the full-scale system and corresponding to 702 data points. Future details regarding surface elevation and damping force are taken into account with a 0.36-second horizon. Subsequently, the output predicts the forthcoming information of the PTO translator position for the next 0.36 s. To construct input and output datasets, all possible

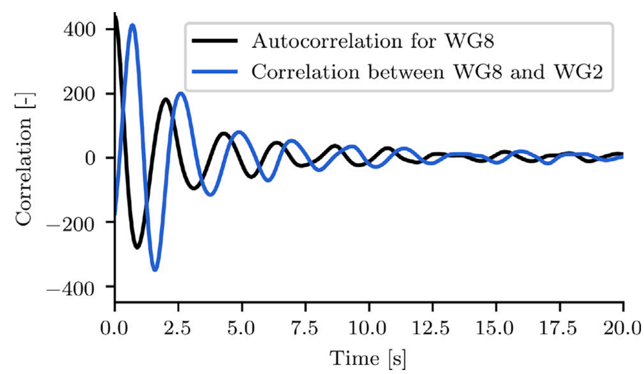

Fig. 8. Auto-correlation function for the WG8 signal, and the correlation function between WG2 and WG8 signals are shown for the 1:30 scaled experimental model.

combinations of time series segments from the PTO translator position, surface elevation, and damping force data are considered across various damping configurations which includes $227945 \times 70\% = 159561$ datasets for training, $227945 \times 10\% = 22794$ for validation, and $227945 \times 20\% = 45589$ for testing.

3.6. Peak force NN model architecture

The architecture details of the CNN network designed for predicting peak line force are meticulously outlined in Table 3. The CNN is structured with multiple convolutional layers, each equipped with 250 filters and 10 kernels, and it integrates the Parametric Rectified Linear Unit (PReLU) activation function. Within this framework, the Conv1D layer performs one-dimensional convolution between the kernels and input layers, resulting in the corresponding output. To downsample feature maps, max pooling is applied by identifying the maximum value in each batch, and global average pooling is used to average across each feature map, effectively reducing spatial dimensions to one. The input features of the CNN encompass forthcoming details about surface elevation, PTO translator position, and PTO sliding friction damping force, enabling the prediction of the peak force for the next 0.36 s.

Table 3
The sequential neural network architecture for the peak line force prediction, refer to [33].

Layer (type)	Output Shape	Number of Parameters
Conv1D	(None, 84, 250)	28,750
Conv1D	(None, 75, 250)	644,000
MaxPooling1D	(None, 37, 250)	0
Conv1D	(None, 28, 250)	632,250
Conv1D	(None, 28, 250)	69,750
GlobalAveragePooling1D	(None, 250)	0
Dropout	(None, 250)	0
Dense	(None, 1)	252
Total Parameters: 1,375,002 (Trainable: 1,375,002, Non-trainable: 0)		

The total datasets contain $4926 \times 70\% = 3448$ datasets for training, $4926 \times 10\% = 492$ for validation, and $4926 \times 20\% = 985$ for testing.

3.7. Loss and accuracy

The accuracy of the system is evaluated using its goodness-of-fit (GOF) measure, defined as:

$$\mathrm{GOF} = 1 - \sqrt{\frac{(\hat{Y}-Y)^T(\hat{Y}-Y)}{Y^TY}} \tag{2}$$

Here, Y and $\hat{Y}$ are column vectors representing the true and predicted values of the output, respectively. The deviation between the predicted output and the true (experimentally measured) data is quantified by:

$$L(\hat{Y},Y) = \sqrt{\frac{(\hat{Y}-Y)^T(\hat{Y}-Y)}{Y^TY}} + R_{L_2} \tag{3}$$

where R_{L_2} is the L_2 regularization term.

3.8. Sensitivity to the prediction of future knowledge

The sensitivity of the force prediction model to the prediction accuracy of surface elevation and PTO translator position is studied.

The predicted surface elevation with different GOF is computed by assuming a noise spectrum similar to the wave spectrum and considering the noise ratio (σ_n/σ_η) as the ratio of standard deviations ranging from 0.1 to 0.5 with the steps of 0.1. The JONSWAP spectrum [38] was taken as the wave spectrum to generate irregular waves for the wave tank experiment:

$$S_J(\omega) = A_\gamma\, S_{\mathrm{PM}}(\omega)\, \gamma^{\exp\left(-0.5\left(\frac{\omega-\omega_p}{\sigma\,\omega_p}\right)^2\right)} \tag{4}$$

where the non-dimensional peak shape parameter is $\gamma = 3.3$, and the spectral width parameters are $\sigma_a = 0.07$ for $\omega \leqslant \omega_p$, and $\sigma_b = 0.09$ for $\omega > \omega_p$. Further, $A_\gamma = 1 - 0.287\ln(\gamma)$ is a normalizing factor. The Pierson–Moskowitz (PM) spectrum S_{PM} is described as:

$$S_{\mathrm{PM}}(\omega) = \frac{5}{16} H_s{}^2 \omega_p{}^4 \omega^5 \exp\left(-\frac{5}{4}\frac{\omega}{\omega_p}\right). \tag{5}$$

To construct the noise spectrum, the significant wave height in Eq. (5) is considered as $H_s = 4\sigma_n$, while the peak angular frequency and shape factor are kept the same as the wave spectrum without noise. Thus, the surface elevation is calculated as a superposition of the angular frequency components:

$$\eta_{\mathrm{noise}}(t) = \sum_i a_i\, cos\left(\omega_i t + \alpha_{i,\mathrm{rand}}\right) \tag{6}$$

$$a_i = \sqrt{2S_J(\omega_i)d\omega} \tag{7}$$

where a_i are the amplitude, and $\alpha_{i,\mathrm{rand}}$ are the randomized phases that are evenly distributed over $]0, 2\pi[$. Then, the generated noise wave elevation is added to the true surface elevation that was measured by wave gauges during the experiment to provide an estimate of an inaccurately predicted surface elevation considering different GOF levels.

In a similar fashion, the noise signal for the PTO translator position is obtained assuming a noise spectrum similar to the PTO translator position spectrum using Fourier transform. Since the PTO translator position signal, $z(t)$, is defined in a finite interval $[-T/2, T/2]$, and assuming that this signal is periodic [39], the Fourier series of the noise can be written as:

$$z_{\mathrm{noise}}(t) = \frac{1}{\mathrm{SNR}} \sum_{n=-\infty}^{\infty} c_n e^{i\omega_n t} \tag{8}$$

where SNR is the signal-to-noise ratio, and c_n is the complex amplitude computed from:

$$c_n = \frac{d\omega}{2\pi}\int_{-T/2}^{T/2} z(t) e^{-i\omega_n t} dt \tag{9}$$

where $\omega_n = n d\omega$ and the fundamental frequency is defined as $d\omega = \frac{2\pi}{T}$. The ratios $1/\mathrm{SNR}$ are defined as 0.001, 0.015, 0.05, 0.12, and 0.2. The different generated noisy signals for the surface elevation and PTO translator position, together with their GOF, are shown in Fig. 9.

4. Autoregressive method

The autoregressive (AR) model is a statistical method widely employed for analyzing time-series data. This model leverages past observations to perform regression analysis, predicting the value of the next time period. Specifically, the AR model assumes that the variable $y(k)$ at time step k is a linear function of its past observations $y(k-1), y(k-2), \ldots, y(k-p)$, where p is the order of the model, in addition to some noise disturbances. Hence, the predicted output $\hat{y}(k|k-1)$ at time step k can be described as [4,9,10]:

$$\hat{y}(k|k-1) = \Phi Y_{k-1,k-p} \tag{10}$$

where $Y_{k-1,k-p}$ is the vector of past observations and Φ is the vector of regression coefficients defined as:

$$Y_{k-1,k-p} = [y(k-1)\; y(k-2)\; \ldots\; y(k-p)]^T \tag{11}$$

$$\Phi = [\varphi_1\; \varphi_2\; \ldots\; \varphi_p].$$

The regression coefficients are constant values determined before the prediction process by minimizing the least square cost function:

$$J = \sum_{k=p+1}^{N} (y(k) - \hat{y}(k|k-1))^2 \tag{12}$$

where, N is the number of past values that the model is trained over. Therefore, the coefficients that minimize the cost function J are identified as:

$$\Phi = (M_{1,N-1}^T M_{1,N-1})^{-1}(M_{1,N-1}^T Y_{p+1,N}) \tag{13}$$

where $M_{1,N-1} \in \mathbb{R}^{(N-P-1)\times p}$

$$M_{1,N-1} = \begin{bmatrix} y(p) & y(p-1) & \ldots & y(2) & y(1) \\ y(p+1) & y(p) & \ldots & y(3) & y(2) \\ \vdots & \vdots & \ddots & \vdots & \vdots \\ y(N-1) & y(N-2) & \ldots & y(N-p+1) & y(N-p) \end{bmatrix} \tag{14}$$

and $Y_{p+1,N} \in \mathbb{R}^{(N-P)\times 1}$

$$Y_{p+1,N} = [y(p+1)\; y(p+2)\; \ldots\; y(N-1)\; y(N)]^T. \tag{15}$$

Lastly, to assess the performance of the model, GOF is derived, the same as in Eq. (2).

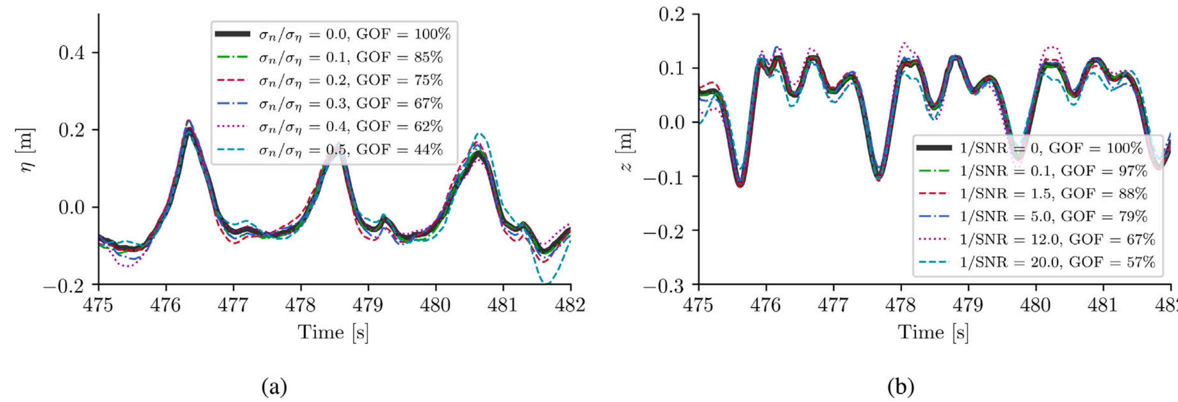

Fig. 9. The surface elevation (η) and PTO translator position signals (z) with different noise levels are shown in (a) and (b), respectively, for the D_0 damping case.

5. Kalman filter method

The time-varying Kalman filter, which is an extension of the steady-state filter designed for time-varying systems or Linear Time-Invariant (LTI) systems, with nonstationary noise covariance is considered. A linear time-invariant model as the foundation of the filtering process is taken by assuming a superposition of N_ω damped harmonic oscillators with constant frequencies and constant damping coefficients. If the Kalman filter aims to estimate the current state of the model, namely the velocity ($\dot{y}$) and position (y) of the harmonic oscillators, the continuous form of the state space and measurement equation can be formulated as [40]:

$$\dot{X}(t) = A'(\omega,\xi)X(t) + B'u(t) + G'W(t) \qquad (16)$$
$$y(t) = C'X(t) + D'u(t) + v(t)$$

Here, $\dot{X}(t) = [\ddot{y}(t)\ \dot{y}(t)]^T$, and W is the vector of white noise with a Gaussian distribution, and G' is the identity matrix with the appropriate dimension. Additionally, ξ represents the damping ratio, and ω is the natural frequency. The measurement noise, $v(t)$, is zero with the assumption that the measured and true data are identical here, and no input is considered in the plant. Considering N_ω number of frequency elements, the matrices $A'(\omega,\xi)$, B', C', and D' are defined as:

$$A'(\omega,\xi) = \begin{bmatrix} \mathrm{diag}\{[-2\omega_i\xi_i]\} & \mathrm{diag}\{[-\omega_i^2]\} \\ I_{N_\omega} & 0_{N_\omega\times N_\omega} \end{bmatrix} \qquad (17)$$
$$B' = I_{2N_\omega}$$
$$C' = \begin{bmatrix} 0_{1\times N_\omega} & 1_{1\times N_\omega} \end{bmatrix}$$
$$D' = 0_{2N_\omega}$$

where I is the identity matrix.

The Kalman filter algorithm ensures that the covariance of the estimated model states is minimized. The continuous plant state and measurement equations can be converted to their discrete form as explained in [41] resulting in [42]:

$$\begin{aligned} X(k+1) &= AX(k) + GW(k), \\ y(k) &= CX(k) + v(k). \end{aligned} \qquad (18)$$

The time-varying Kalman filter goes through the following update equations:

- Measurement update:

$$\begin{aligned} \hat{X}(k|k) &= \hat{X}(k|k-1) + K(k)(y(k) - C\hat{X}(k|k-1)), \\ K(k) &= P(k|k-1)C^T(R(k) + CP(k|k-1)C^T)^{-1}, \\ P(k|k) &= (I - K(k)C)P(k|k-1), \end{aligned} \qquad (19)$$

- Time update:

$$\begin{aligned} \hat{X}(k+1|k) &= A\hat{X}(k|k) \\ P(k+1|k) &= AP(k|k)A^T + GQ(k)G^T. \end{aligned} \qquad (20)$$

Here, $\hat{X}(k|k-1)$ is the estimate of $X(k)$ given the past measurements up to y(k-1) and $\hat{X}(k|k)$ is the updated estimate based on the last measurement $y(k)$. Additionally:

$$\begin{aligned} Q(k) &= E(W(k)W(k)^T), \\ R(k) &= E(v(k)v(k)^T). \end{aligned} \qquad (21)$$

With initial conditions $\hat{X}(1|0)$ and $P(1|0)$, the filtering process involves iteratively applying these equations ensuring update both the state estimates $\hat{X}$ and error covariance P matrices at each time sample. Knowing the state estimate $\hat{X}(k|k)$, the n-step ahead prediction, $\hat{y}(k+n)$, can be simply calculated as:

$$\hat{y}(k+n) = CX(k+n) = CA^n\hat{X}(k|k). \qquad (22)$$

6. Results and discussion

6.1. Surface elevation DNN prediction

The surface elevation prediction model has converged after 241 epochs with 95% accuracy and 0.05 loss for both the training and validation dataset. The predicted surface elevation captures the measured surface elevation very well, see Fig. 10. To construct the whole predicted surface elevation signal, the length of the measured data is divided in windows of 0.36 s, and the surface elevation for each window is predicted from the *measured* history of the signals from wave gauges 8 and 2. Since the windows adopted here are not overlapping, the predicted signal can be constructed by concatenating all predicted windows.

6.2. PTO translator position DNN prediction

The network performance for the predicted PTO translator position signal gives an accuracy of 92% and 87% as well as a loss of 0.08 and 0.13 for the training and validation dataset, respectively, after 322 epochs. A comparison of the predicted PTO translator position with the true and predicted surface elevation as its input is elucidated in Fig. 11. The whole predicted PTO translator position signal is obtained in a similar way as the predicted surface elevation explained in Section 6.1. The results indicate that the network's performance drops as the damping increases. This drop in the prediction accuracy may be avoided by categorizing the damping range to, for instance, low, average, and high, and training separate models for each category. This approach particularly allows the model to be trained over similar system behavior, therefore, providing better accuracy for each range of damping. However, this approach requires much larger training data and more damping cases than the one studied here. In general, larger training data leads to better accuracy of the data-driven models.

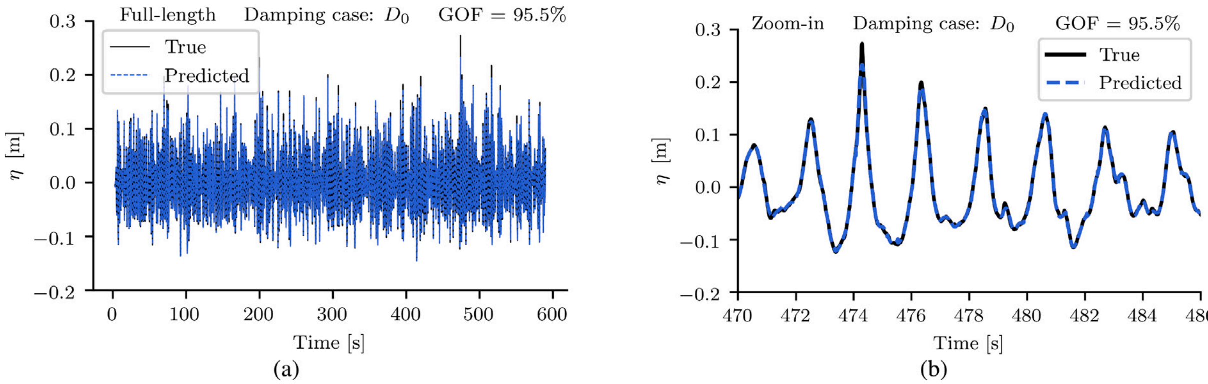

Fig. 10. The predicted surface elevation from the DNN model for D_0 damping case for the 1:30 scaled system.

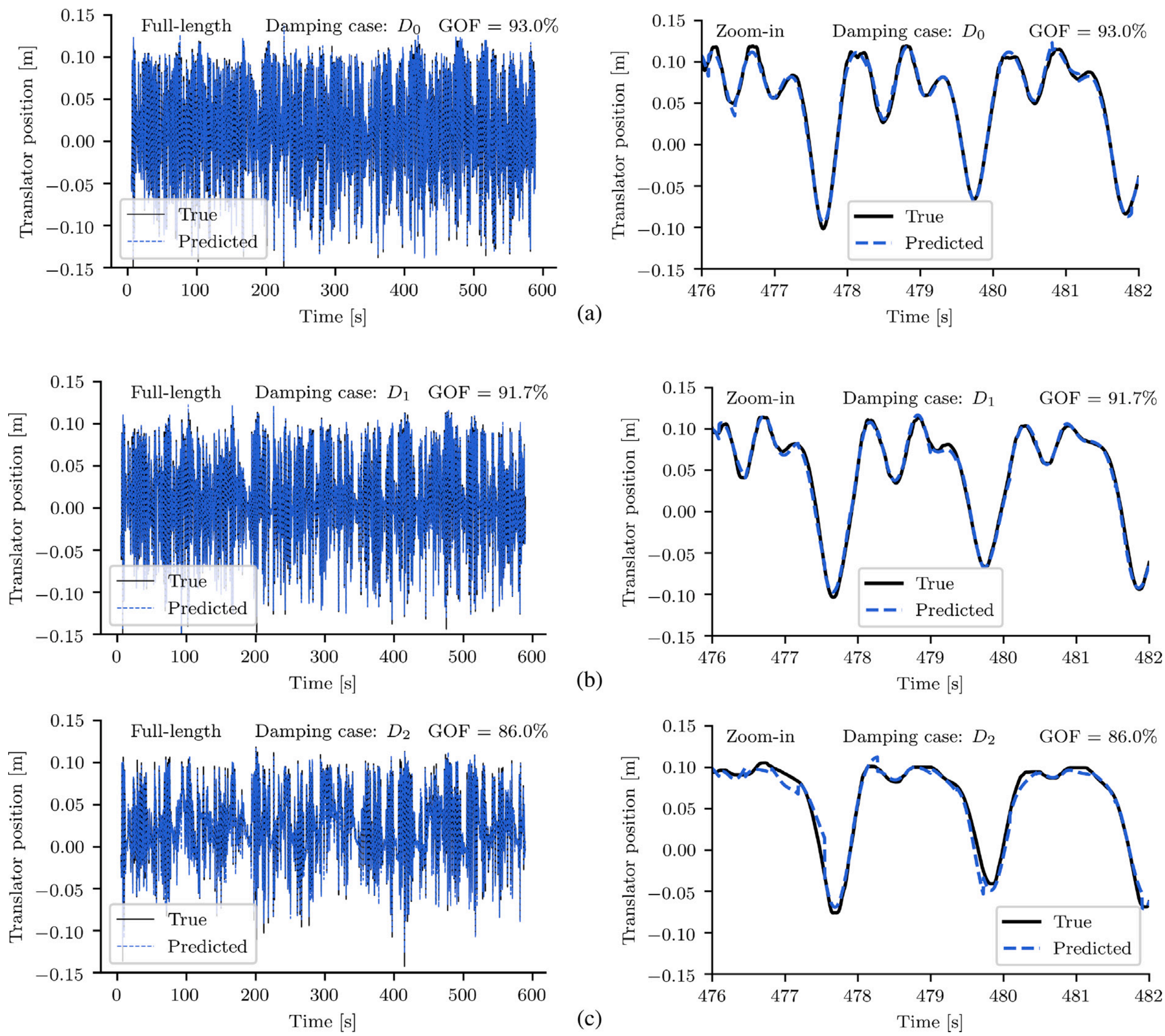

Fig. 11. The predicted PTO translator position from the DNN model for the damping cases D_0, D_1, and D_2 is shown in (a), (b), and (c), respectively, for the 1:30 scaled system.

6.3. Peak force CNN prediction

The training and validation accuracy of the peak force prediction is 91% and 89%, with a loss of 0.09 and 0.11, respectively, after 106 epochs, see Fig. 12.

Fig. 13 shows the quantile plot of the true and predicted peak line force for the *test dataset* with an accuracy of 90.3%. In other words, the predicted peak line force is computed based on the true surface elevation and PTO translator position. The figure indicates a good model performance as the data points fall close to the diagonal line.

Fig. 14 depicts the network performance when the *predicted* surface elevation and PTO translator position are given as the input to the model. The accuracy of the peak force prediction has dropped by about 7% for the D_0 and D_1 damping cases, in comparison to Fig. 13 where the true inputs were given to the model. Nevertheless, the model shows

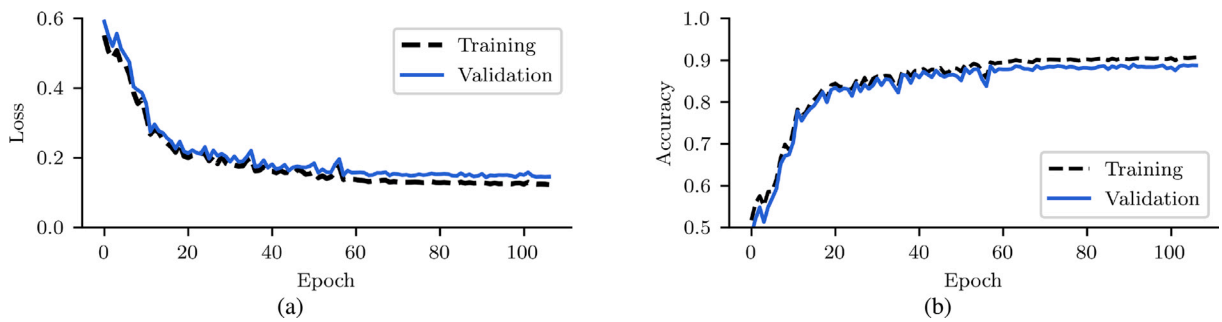

Fig. 12. Loss and accuracy (GOF) of the CNN model for peak force prediction for the 1:30 scaled system.

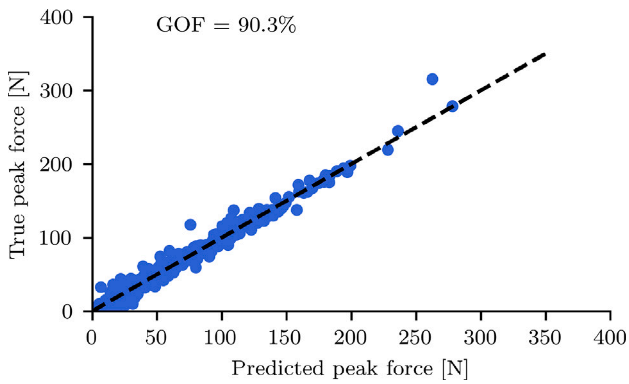

Fig. 13. The quantile plot for the CNN model shows the correlation between the predicted and measured peak force of experimental data, i.e. the test dataset for all damping configurations.

quite a satisfactory correlation, even though its input was given by the predicted signals. However, for the D_2 damping case, the performance has dropped more significantly to an accuracy of 75.6%. A performance drop was expected due to lower prediction accuracy for this damping case which may be avoided if a more specific network was designed for larger damping cases and if more experimental data was available as explained in Section 6.2.

Another common indicator of the model performance is the correlation between the true and predicted signal: $C_r = c_{12}/\sqrt{c_{11}c_{22}}$, in which c_{ij} are the elements of the covariance matrix. Accordingly, besides the GOF, the correlation for Fig. 13, and Fig. 14(a), (b), and (c) are computed as 99%, 96.6%, 96.5%, and 89.2%, respectively.

The accuracy of the peak force prediction model is further investigated by filtering the predicted PTO translator position using a low-pass filter where the filter order, critical frequency, and sampling frequency are considered as 4, 3 rad/s, and 300 Hz, respectively. The filtering of the PTO translator position slightly smoothens the predicted signal and contributed to only a 0.5% to less than 1.0% increase in the accuracy of predicted peak forces, and thereby, it is considered ineffective here. Note that the results presented in this paper are without filtering the PTO translator position signal.

6.4. Autoregressive and Kalman filter performance

The prediction accuracy of AR and KF methods has been studied for surface elevation and PTO translator position for different fixed PTO system setup. The prediction horizon, considered the same as NN models, is set to 0.36 s (equivalent to 2 s for the full-scale system).

The assessment of the autoregressive model's performance is followed by considering the influence of low-pass filtering on the signal. Following the suggestion by Fusco and Ringwood 2010 [4], filtering significantly enhances signal prediction accuracy, attributed to the concentration of a substantial portion of wave energy at low frequencies, as depicted in Fig. 4. Notably, it has been observed that the predicted signal demonstrates a high sensitivity to the cut-off frequency value, suggesting the importance of identifying an optimal value that is neither too low nor too high to maximize the AR model's performance. As a result, low-pass filtering is applied with a chosen cut-off frequency of 3.2 Hz in this study. To ensure a precise evaluation of the predicted signal, the GOF is computed based on the measured unfiltered signal.

Table 4
The time-varying KF prediction accuracy of surface elevation signal for various numbers of frequency components is shown.

	$N_\omega = 10$	$N_\omega = 20$	$N_\omega = 30$	$N_\omega = 100$	$N_\omega = 200$
GOF	10.9%	27.3%	31.4%	32.3%	31.7%

The AR model's performance is comprehensively evaluated across various training periods ($N \times T_s$) and the model order presented by its equivalent period ($p \times T_s$). The results are presented for a constant sampling period of 0.0039 s. Generally, increasing the training period enhances prediction accuracy across all model orders. However, the impact of increasing p exhibits a nuanced trend. An optimal model order exists, delivering peak predictive performance, as illustrated in Figs. 15 and 16. Remarkably, further escalating the model order does not necessarily yield improved GOF. Notably, the optimal model order, yielding the highest GOF, varies for the PTO translator position across different damping configurations, as illustrated in Fig. 16.

Fig. 17 investigates the resampling impact on the accuracy of the AR model applied to surface elevation and PTO translator position data. The resampling, with a variable sampling period ranging from [1/256, 1/3] s and steps of 0.005 s, aims to systematically assess the AR model's performance across different sampling resolutions. The chosen equivalent periods for the model order ($p \times T_s$) and training period ($N \times T_s$) are held constant throughout all resampled datasets. For surface elevation, $p \times T_s$ is set at 1.56 s, and for translator position signals under damping configurations D_0, D_1, and D_2, it is considered as $p \times T_s = [1.56, 3.91, 1.56]$ s, respectively. The optimal training period of 30 s is identified for both surface elevation and the PTO translator position signals, as illustrated in Fig. 15 and Fig. 16.

For the time-varying Kalman filter method, computational limitations dictated the adoption of a minimum sampling period of 0.039 s, as lower values were not feasible within standard laptop settings. Furthermore, the observation was made that an initial increase in the number of frequency components during Kalman filter analysis enhances the GOF. However, beyond a certain threshold, additional increments in the number of frequencies show negligible impact. An example of this sensitivity is presented for the predicted surface elevation signal, as shown in Table 4. For this study, 100 frequency components have been considered. Additionally, a constant damping coefficient of 0.025 for all harmonics, and a small input noise covariance matrix of $Q = 0.002 I_{2N_\omega}$ are chosen to ensure filter stability.

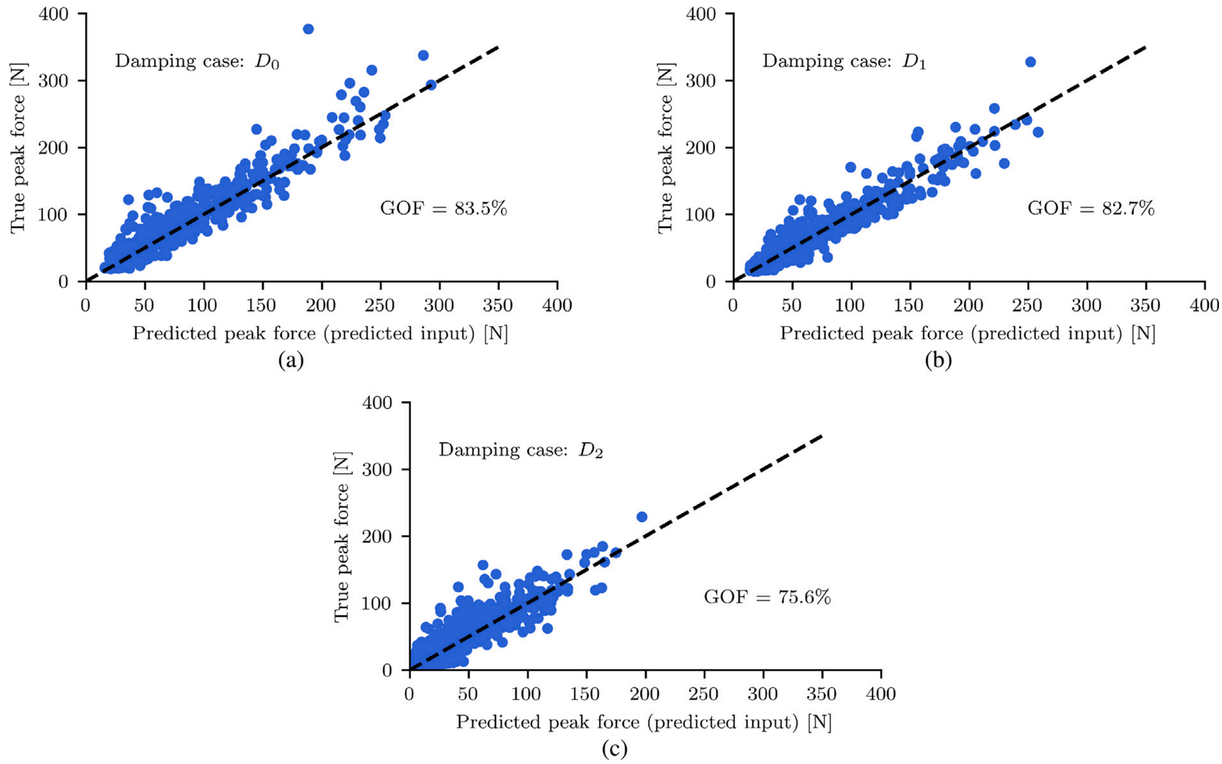

Fig. 14. The quantile plot of the measured peak force with the predicted one based on the predicted surface elevation and PTO translator position in the CNN model for the damping cases D_0, D_1, and D_2 is shown in (a), (b), and (c), respectively, for the 1:30 scaled system.

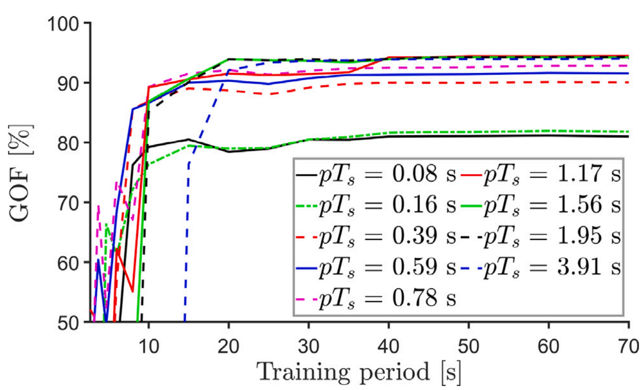

Fig. 15. The sensitivity of the AR model to training period ($N \times T_s$) and equivalent periods for the model order ($p \times T_s$) is demonstrated for surface elevation prediction. The sampling frequency of 256 Hz ($T_s = 0.0039$ s) is considered.

The comparison of prediction accuracies for AR, KF, and NN models is presented in Table 5. Notably, a marked enhancement in AR prediction is achieved through data filtering, consistent with findings in [4]. In contrast, the time-varying Kalman filter exhibits poor prediction performance, aligning with the observations reported in [4] for the Kalman filter methods studied therein.

It is crucial to note that the AR and KF models focus solely on predicting the PTO translator position signal under a fixed PTO damping configuration in each analysis. Conversely, the DNN model employed for PTO translator position prediction undergoes initial training across all available damping configurations, enabling subsequent predictions for any desired damping value. This distinction is particularly crucial as the classical models, such as AR, fall short when attempting to forecast data under varying control inputs, such as changes in PTO damping, which result in alterations to the system behavior and translator position signal. Here, a key objective of the control strategy is to directly predict the future system state based on its control input, eliminating the need for extensive model training or lookup table creation, as required by multiple AR models, to achieve satisfactory predictions for diverse control inputs.

The data-driven models exhibit a substantial advantage over classical approaches due to their intrinsic ability for non-linear modeling without reliance on assumptions about the statistical distribution governing observations. It is crucial to select an appropriate prediction horizon length for a realistic control scheme. While an excessively long prediction horizon may prove unnecessary, assuming a too-short horizon may not align with the practicalities of the system. Consequently, the selection of the prediction horizon length for this study has been made by carefully considering the prediction accuracy and suitable forecasting horizon. Here, NN models, when provided with sufficient data, demonstrate the capability to fulfill the prediction requirements.

For systems requiring precise prediction of mooring forces, classical approaches utilizing Kalman filtering can prove effective, particularly when the system dynamics are well-defined through mathematical expressions. However, the friction-based PTO system considered in this study presents a challenge in accurately representing its highly nonlinear behavior within the dynamic equations. The elusive nature of accurately defining the system dynamics poses a risk of severe modeling errors and inaccurate predictions of the line force. Therefore, the KF method considering PTO system dynamics in its state space equation has not been applied to predict mooring forces in this context. Here, the superiority of NN models is emphasized once again, as they allow an accurate model-free prediction of the next instant. The rest of the analysis in the following sections is performed based on predicted data using NN models.

6.5. Sensitivity to prediction horizon for various NN models

Another parameter that affects the prediction GOF of all the networks is the length of the prediction horizon. The length of 0.36 s, i.e. 2 s in the full-scale system, is considered to be a compromise between the

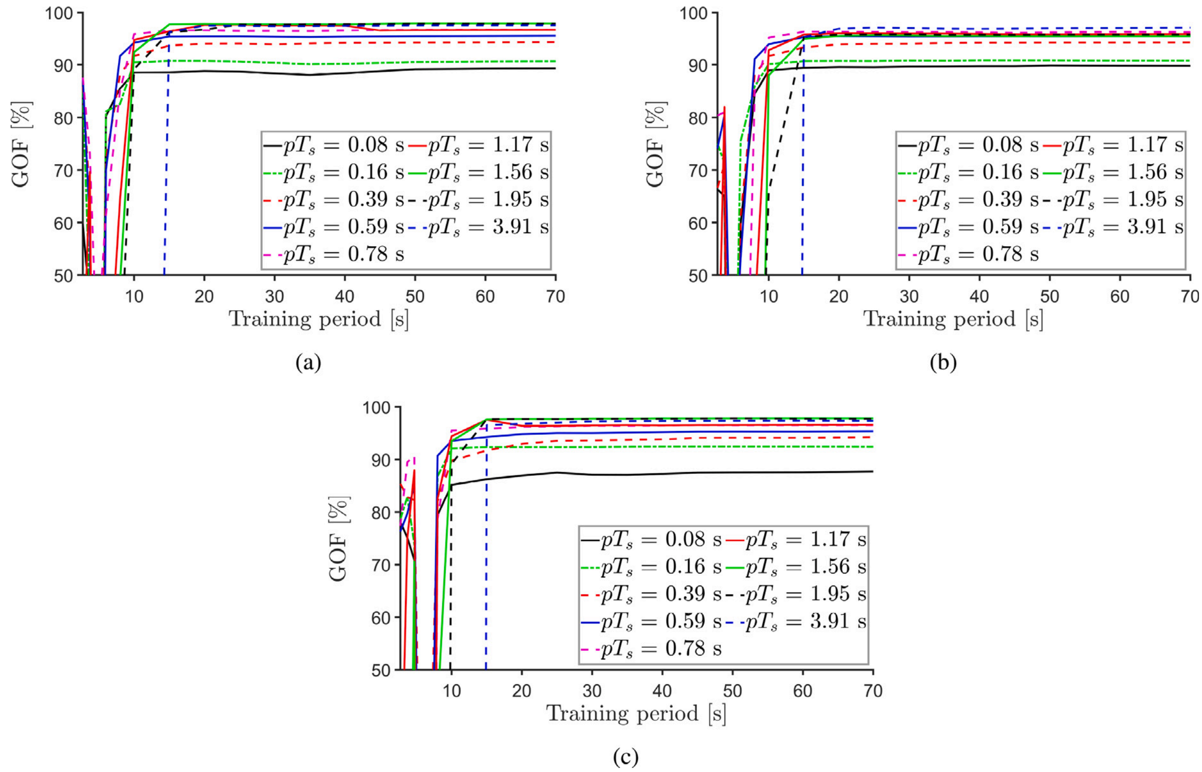

Fig. 16. The sensitivity of the AR model to training period ($N \times T_s$) and equivalent periods for model order ($p \times T_s$) for predicting PTO translator position signals are shown for damping cases D_0, D_1, and D_2 in (a), (b), and (c), respectively. The sampling frequency of 256 Hz (i.e. $T_s = 0.0039$ s) is considered.

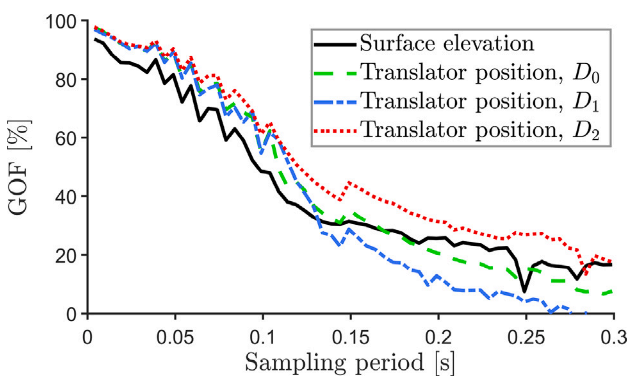

Fig. 17. Sensitivity of the AR model to the sampling period is shown for the prediction of surface elevation and PTO translator position signals.

Table 5
A comparison of the GOF among various prediction models is provided.

Data		Prediction model accuracy			
		AR (no filter)	AR (filtered)	KF	NN
Surface elevation		57%	93.7%	32.3%	95.5%
	D_0	71.5%	97.7%	45.8%	93%
Translator position	D_1	70.3%	97%	44.4%	91.7%
	D_2	74.8%	97.7%	59.2%	86%

network accuracy and the allowable delay in the response of the control system to adjust the damping force. The lower the horizon, the higher the networks' prediction accuracy but also the higher the demand on the control system. On the other hand, increasing the prediction horizon provides more time for the WEC to adjust its damping, even though the optimal damping value might not have been accurately predicted.

Fig. 18 shows the accuracy (GOF) sensitivity of the surface elevation, PTO translator position, and peak force prediction models to different prediction horizons ranging from 0.18 to 1.3 s with steps of 0.36 s, i.e. corresponding to the range of 1.0 to 7.0 s with steps of 2.0 s in the full-scale system. The history time of 2.7 s, corresponding to 702 data points, is considered for the surface elevation and PTO translator position prediction models and kept unchanged when varying the prediction horizon, refer to Section 3.4. For all the prediction models in this figure, the measured (true) data is given as the input to the networks. The results illustrate a high dependency of the PTO translator position accuracy to the prediction horizon whereas the prediction time increases, the accuracy decreases monotonously. On the other hand, the accuracy of the surface elevation and peak line force prediction is insensitive to the length of the prediction horizon. This implies that the peak line force prediction CNN model is able to predict the peak forces for a much longer horizon with small or no compromise in its precision, provided that the PTO translator position is accurately predicted.

6.6. Sensitivity to uncertainties within the prediction of surface elevation and PTO translator position

The sensitivity of the accuracy of the peak force prediction model to the input parameters with different noise levels is assessed in Fig. 19. Here, the effect of prediction accuracy in each input data (i.e. the surface elevation and PTO translator position) is studied separately meaning that the effect of the noisy surface elevation on the GOF of the translator position is not included. As the figure displays, the system is insensitive to the prediction accuracy of surface elevation. In other words, the uncertainties in the prediction of wave elevation do not adversely affect the peak force prediction as long as the translator position prediction accuracy is not compromised. Note that the variation shown in the GOF for surface elevation between different dampings is due to generating the noise signals based on random phase as described in Eq. (6). The network is notably sensitive to the prediction accuracy of

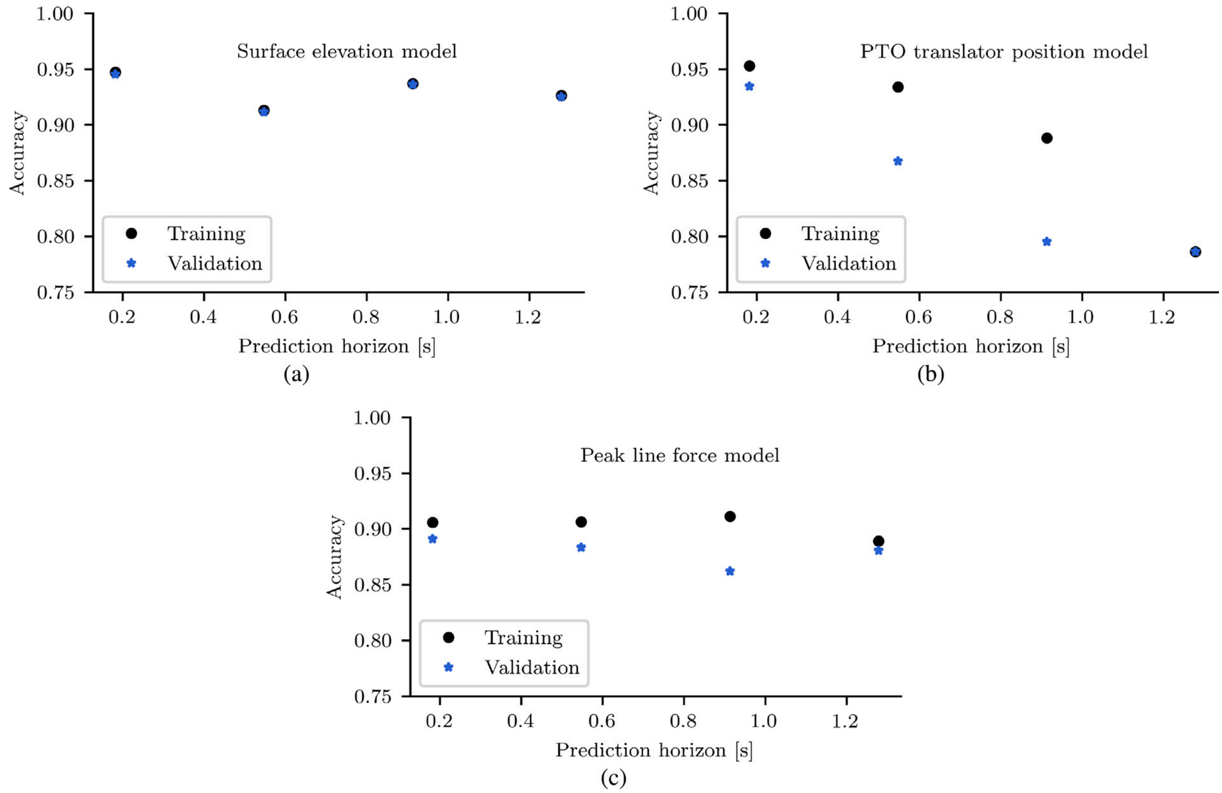

Fig. 18. The sensitivity of the surface elevation, PTO translator position, and peak force prediction models for the training and validation datasets to different prediction horizons is shown in (a), (b), and (c), respectively, for the 1:30 scaled system.

the PTO translator position. This figure illustrates that as the damping increases, the force prediction model is less sensitive to the prediction accuracy of the PTO translator position. Moreover, the lower damping cases of D_0 and D_1 depict a linear trend with respect to the prediction accuracy of the PTO translator position, whereas such a pattern is not seen for D_2. For instance, the prediction accuracy of around 60% and 70% for the PTO translator position resulted in a similar GOF of the predicted peak forces in the D_2 configuration.

6.7. Sensitivity of the optimal damping to the uncertainties in the prediction of PTO translator position

By giving different damping values to the peak force prediction model, the damping that results in the minimum peak force is identified as the optimal damping for each window of 0.36 s of the line force signal. The distribution of the optimal damping value (i.e. the sliding friction force) is illustrated in Fig. 20 for different prediction accuracy of the PTO translator position while the surface elevation signal is the same throughout and is predicted based on Section 6.1. As the predicted translator position signal becomes inaccurate, the model estimates higher damping values to give the minimum peak force. When no error is present in the predicted PTO translator position, the lower damping configuration, i.e. near zero, has the highest chance to result in the minimum peak force. This finding complies with our earlier results presented in [35], where optimum damping values were presented for a DNN model given seven sea states. In [28], we showed that the D_2 case leads to the lowest peak force when looking at the entire 10 min of the sea state duration in the wave tank, refer to Fig. 12 therein. This is not against the findings in this study or in [35], where the optimal damping probability distribution is shown when the signal is broken down to intervals of a few seconds. In other words, the results in this paper and in [35] look at the statistical distribution of the optimal damping value for all short time interval windows, while [28] considers only the highest and most damaging peak line force in the entire sea state. Therefore, this suggests that for increased survivability, lower damping should be applied significantly more often than higher damping.

Again looking at Fig. 20, as the error in the predicted translator position increases, a sliding friction force around the one in the D_2 configuration is estimated to be the more frequent optimal damping value. Note that the sliding friction forces above 18.9 N (corresponding to the D_2 damping configuration in the wave tank experiment) are outside the training range of the network and may therefore be subjected to inaccuracies.

6.8. Implementation in a real WEC control system

The majority of classical approaches to the control problem are model-based, involving the simplification of models for tractable computation and analysis. The effectiveness of control performance in these model-based approaches is intricately linked to the chosen model fidelity. Severe modeling errors, which may result from parametric issues or unaccounted dynamics, have the potential to introduce unpredictable behavior in the device, possibly leading to damage. On the other hand, high-fidelity models may pose challenges in achieving real-time control solutions due to high computational time. As a consequence, the model-based approach can be susceptible to errors, especially in highly nonlinear dynamics and extreme sea states. Nonlinear Model Predictive Control (NMPC) is introduced as a more realistic scheme; however, its implementation entails a high level of complexity and often necessitates extensive computational time, along with time-consuming optimization loops [43]. Consequently, there is a growing interest in control strategies based on system data in control synthesis, influenced by data availability, control objectives, and the type of application [44–47]. Thus, the distinguishing feature of data-driven methods lies in their intrinsic capacity for non-linear modeling, devoid of any assumptions regarding the statistical distribution governing the observations.

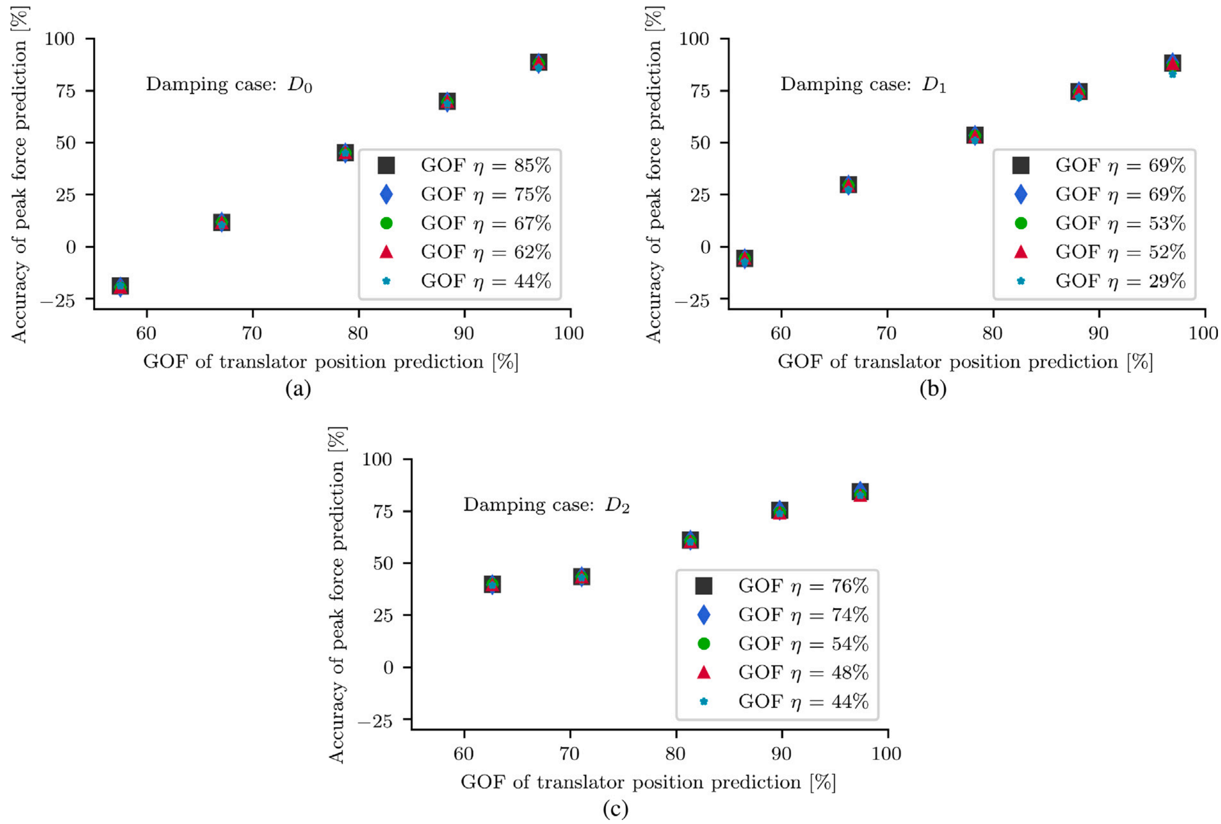

Fig. 19. The sensitivity of the peak force prediction to the uncertainties in the surface elevation and PTO translator positions for the damping cases D_0, D_1, and D_2 is shown in (a), (b), and (c), respectively, for the 1:30 scaled system.

Hence, the proposed survivability model introduces a model-free control scheme, offering a realistic approach for operating the device in a highly nonlinear environment where modeling the system may pose challenges. It is noteworthy that the majority of currently presented control strategies focus solely on heave motion, unlike the approach undertaken here. Moreover, while most model-based strategies typically consider a simple linear generator with a spring–damper working principle, this study employs a friction-based PTO system with highly nonlinear dynamics. However, these nonlinearities are not necessarily drawbacks for the purpose of this study, as real systems often exhibit dissipative losses, resulting in somewhat nonlinear dynamics compared to ideal cases. For the survivability model proposed here, the future knowledge of the incoming waves and system state (i.e. PTO translator position) is necessary to predict the peak line force a few seconds ahead. The analysis here suggests that the CNN model is capable of predicting the peak forces with high accuracy. However, it is particularly dependent on the precision of the predicted PTO translator position. Although this may be seen as a disadvantage, once the PTO translator position network is trained over a relatively large amount of data for various damping values, it is able to quickly and accurately feed the CNN prediction model of the peak forces.

In comparing different neural network model architectures, the LSTM network is often favored for time series prediction due to its ability to retain the memory of past data, enabling it to capture significant long-term dependencies and accommodate inputs of varying lengths. However, one drawback of LSTM networks of comparable size and parameter count to the DNNs examined in this study is their extended training duration. Conversely, conventional DNNs typically require less time for training. It is important to note that the training duration of a model is influenced by several factors, such as hardware setup and model complexity. In our analysis, the historical length used in predicting surface elevation and PTO position is carefully selected to capture temporal dependencies in the data. However, increasing this historical length has not notably enhanced the network's prediction performance, suggesting a lack of strong long-term dependency in the data. Moreover, visual examination of the autocorrelation results, depicted in Fig. 8, reveals a weak dependency of the signal on its delayed copy at longer lags beyond 15 s. In the context of predicting the PTO translator position, our study aims to elucidate the relationship between the PTO damping parameter and the system's response. With noticeable differences observed in the dynamic response across the three damping configurations under investigation, the dependency of the PTO translator position on past datasets is confined to the historical data associated with each specific damping configuration. Consequently, the appeal of capturing long-term dependencies across the input datasets and across different damping configurations is diminished.

The survivability strategies may include the reduction of other forces induced on the structure besides the mooring line. For instance, excessive over-topping may result in forces that target the WEC hull and can be of special importance for the devices that the mechanical or electrical components are installed in the hull of the wave energy converter. This aspect has not been studied here and it is the scope of future work.

In the context of predicting wave elevation, it is noteworthy that the assumption considered here is similar to [4] and relies exclusively on historical data collected at a specific point on the sea surface. This approach offers a significant advantage in terms of model simplicity and reduced instrumentation requirements. Such a strategy is particularly advantageous for unidirectional devices, such as specific types of WECs, which inherently do not require accounting for multidirectionality and radiation effects. This reduction in complexity and instrumentation needs enhances the overall attractiveness of this approach, necessitating measurements at only a single point. Furthermore, there is an alternative methodology for predicting surface elevation, which involves using data obtained from a set of distant measurement instruments positioned in the proximity of the WEC device. However,

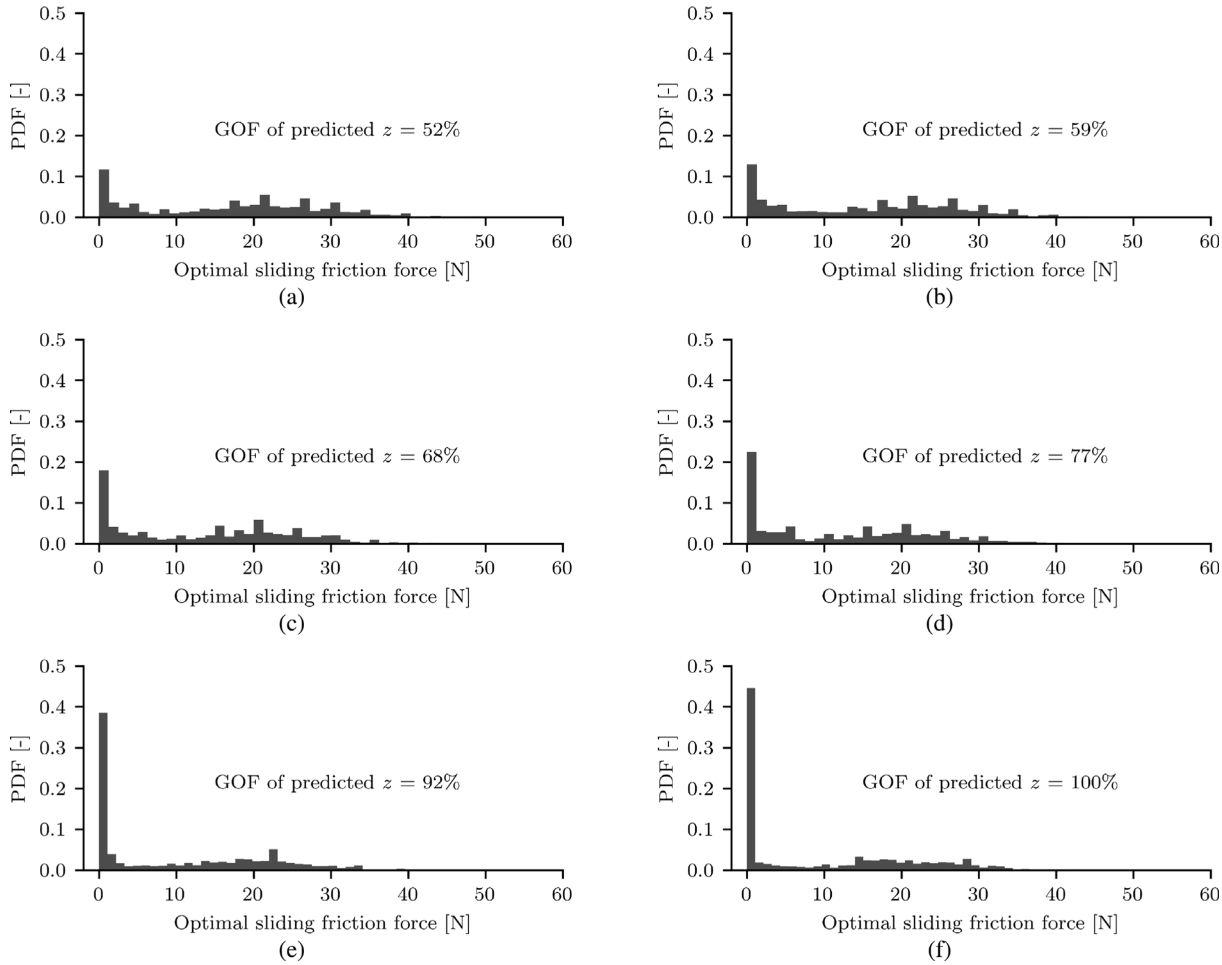

Fig. 20. The probability density function of the optimal damping for different prediction accuracy of the PTO translator position.

it is crucial to acknowledge that this alternative approach introduces additional complexities and instrumentation demands [4].

Further note that the utilization of Froude scaling in wave tank experiments for scaled models does not exert an influence on the final results when considering the full-scale system. The data, before its integration into the neural network, is normalized as elaborated in Normalization 3.2. Even though the initial dataset originates from scaled models, the data undergoes additional normalization procedures. Therefore, the outcome remains unaffected by the scale of the initial data, resulting in consistent network performance for the full-scale device.

7. Conclusion

In the survivability of wave energy converters (WECs), the strategy to reduce the line force by finding the optimum damping may rely on the prediction of future knowledge of force, system state, and incoming waves. The prediction of future data implies the existence of uncertainties within the computational process. However, depending on the strategy adopted for the data-driven approach, these uncertainties may not necessarily result in an inaccurate estimation of optimum damping value.

The deep neural network (DNN) model for the prediction of surface elevation achieves 95.5% goodness-of-fit (GOF) for a prediction horizon of 0.36 s, i.e. 2 s in the full-scale system. The PTO translator position prediction using the DNN model obtains 93%, 92%, and 86% accuracy (GOF) for damping cases of D_0, D_1, and D_2, respectively, for the same prediction horizon as surface elevation that is 0.36 s. The convolutional neural network (CNN) accurately predicts peak forces with approximately 90% precision within a 0.36-second horizon when provided with true (measured) data as input. However, when the predicted surface elevation and PTO translator position are supplied to the model for damping cases represented by D_0 and D_1, the accuracy experiences a decrease of around 7%. Notably, the decline in accuracy is more pronounced for the D_2 damping case.

This study also rigorously compares the performance of the neural network prediction models with classical autoregressive (AR) and Kalman filter (KF) methods in predicting surface elevation and PTO translator position. While AR demonstrates a marginal superiority in fixed PTO configurations, its inherent limitation lies in its incapacity to adapt to real-time variations in system parameters. This deficiency impedes its practical applicability in accurately predicting the output signal based on the dynamic changes in system parameters; a capability that is essential for understanding how the future system output evolves when subjected to arbitrary control inputs. In contrast, neural networks, by establishing a comprehensive relationship between system parameters and future system behavior, provide a robust model for addressing this predictive challenge. Significantly, for continuous control inputs, the neural network outperforms classical methods, highlighting its capability with minimal training on specific configurations. If classical prediction methods such as AR are to be adopted, the creation of the lookup tables is necessary to select appropriate predictive models based on a wide range of system parameters. This would also imply that a large number of pre-trained models for various system configurations are needed, requiring extensive computational time and simulation of system behaviors.

Through sensitivity analysis, the results reveal that the uncertainty in wave elevation prediction has a negligible direct impact on forecasting peak line forces. The CNN model for peak line force exhibits a significantly stronger dependence on the PTO translator position as its input data. The sensitivity study of the peak force model to different noise levels in the input data indicates that the larger damping configuration of D_2 is less sensitive to uncertainties in predicting the PTO translator position.

Furthermore, a sensitivity study to the prediction horizon shows a monotonous decrease in the PTO translator position prediction GOF as the prediction horizon extends. On the other hand, the peak line force and surface elevation prediction models are nearly insensitive to the prediction horizon.

The results show that as the GOF of the PTO translator position drops, sliding friction damping forces between 15 to 30 N are more frequently identified as the optimal damping unlike what a perfect translator position prediction suggests.

CRediT authorship contribution statement

Zahra Shahroozi: Conceptualization, Methodology, Software, Formal analysis, Writing – original draft. **Malin Göteman:** Supervision, Review & editing, Funding acquisition. **Jens Engström:** Supervision, Review & editing, Funding acquisition.

Declaration of competing interest

The authors declare that they have no known competing financial interests or personal relationships that could have appeared to influence the work reported in this paper.

References

[1] Seongho Ahn, Kevin A. Haas, Vincent S. Neary, Wave energy resource characterization and assessment for coastal waters of the United States, Appl. Energy 267 (2020) 114922.

[2] Zahra Shahroozi, Malin Göteman, Jens Engström, Fatigue analysis of a point-absorber wave energy converter based on augmented data from a WEC-Sim model calibrated with experimental data, Trends Renew. Energ. Offshore (2022) 925–933.

[3] Mohammed A.A. Desouky, Ossama Abdelkhalik, Wave prediction using wave rider position measurements and NARX network in wave energy conversion, Appl. Ocean Res. 82 (2019) 10–21.

[4] Francesco Fusco, John V. Ringwood, Short-term wave forecasting for real-time control of wave energy converters, IEEE Trans. Sustain. Energy 1 (2) (2010) 99–106.

[5] Bradley A. Ling, Belinda A. Batten, Real time estimation and prediction of wave excitation forces on a heaving body, in: International Conference on Offshore Mechanics and Arctic Engineering, vol. 56574, American Society of Mechanical Engineers, 2015, V009T09A017.

[6] Zahra Shahroozi, Force Prediction and Estimation for Point Absorber Wave Energy Converter (Master's thesis), Uppsala University, 2019.

[7] Kumars Mahmoodi, Erivelton Nepomuceno, Abolhassan Razminia, Wave excitation force forecasting using neural networks, Energy 247 (2022) 123322.

[8] Francesco Paparella, Kieran Monk, Victor Winands, MFP Lopes, Daniel Conley, John V Ringwood, Benefits of up-wave measurements in linear short-term wave forecasting for wave energy applications, in: 2014 IEEE Conference on Control Applications, CCA, IEEE, 2014, pp. 2048–2053.

[9] Yerai Pena-Sanchez, John Ringwood, A critical comparison of AR and ARMA models for short-term wave forecasting, in: Proceedings of the 12th European Wave and Tidal Energy Conference 27th Aug-1st Sept 2017, (961) European Wave and Tidal Energy Conference 2017, 2017, pp. 1–6.

[10] Hoai-Nam Nguyen, Paolino Tona, Short-term wave force prediction for wave energy converter control, Control Eng. Pract. 75 (2018) 26–37.

[11] Ming Ge, Eric C. Kerrigan, Short-term ocean wave forecasting using an autoregressive moving average model, in: 2016 UKACC 11th International Conference on Control, CONTROL, IEEE, 2016, pp. 1–6.

[12] Marco P. Schoen, Jø rgen Hals, Torgeir Moan, Wave prediction and robust control of heaving wave energy devices for irregular waves, IEEE Trans. Energy Convers. 26 (2) (2011) 627–638.

[13] Marina Garcia-Abril, Francesco Paparella, John V. Ringwood, Excitation force estimation and forecasting for wave energy applications, IFAC-PapersOnLine 50 (1) (2017) 14692–14697.

[14] Peter Kracht, Sebastian Perez-Becker, Jean-Baptiste Richard, Boris Fischer, Performance improvement of a point absorber wave energy converter by application of an observer-based control: Results from wave tank testing, IEEE Trans. Ind. Appl. 51 (4) (2015) 3426–3434.

[15] Francesco Fusco, John V. Ringwood, A simple and effective real-time controller for wave energy converters, IEEE Trans. Sust. Energy 4 (1) (2012) 21–30.

[16] Sanil Mhatre, Application of a Linear Optimal Estimator on a Wave Energy Converter Using Bang-Singular-Bang Control (Ph.D. thesis), Michigan Technological University, 2017.

[17] John V. Ringwood, Giorgio Bacelli, Francesco Fusco, Energy-maximizing control of wave-energy converters: The development of control system technology to optimize their operation, IEEE Control Syst. Mag. 34 (5) (2014) 30–55.

[18] Enrico Anderlini, David IM Forehand, Paul Stansell, Qing Xiao, Mohammad Abusara, Control of a point absorber using reinforcement learning, IEEE Trans. Sustain. Energy 7 (4) (2016) 1681–1690.

[19] E Anderlini, DIM Forehand, E Bannon, Q Xiao, M Abusara, Reactive control of a two-body point absorber using reinforcement learning, Ocean Eng. 148 (2018) 650–658.

[20] Leila Ghorban Zadeh, Ali Shahbaz Haider, Ted K.A. Brekken, Bayesian actor-critic wave energy converter control with modeling errors, IEEE Trans. Sustain. Energy 14 (1) (2022) 3–11.

[21] Ted K.A. Brekken, On model predictive control for a point absorber wave energy converter, in: 2011 IEEE Trondheim PowerTech, IEEE, 2011, pp. 1–8.

[22] Jørgen Hals, Johannes Falnes, Torgeir Moan, Constrained optimal control of a heaving buoy wave-energy converter, J. Offshore Mech. Arct. Eng. 133 (1) (2011).

[23] Guang Li, Mike R. Belmont, Model predictive control of sea wave energy converters–Part II: The case of an array of devices, Renew. Energy 68 (2014) 540–549.

[24] Amin Ghadami, Bogdan I. Epureanu, Data-driven prediction in dynamical systems: recent developments, Phil. Trans. R. Soc. A 380 (2229) (2022) 20210213.

[25] Shaswat Saincher, Jyotirmay Banerjee, Influence of wave breaking on the hydrodynamics of wave energy converters: A review, Renew. Sustain. Energy Rev. 58 (2016) 704–717.

[26] Shan Wang, Carlos Guedes Soares, Review of ship slamming loads and responses, J. Mar. Sci. Appl. 16 (4) (2017) 427–445.

[27] Jens Peter Kofoed, Wave Overtopping of Marine Structures: Utilization of Wave Energy (Ph.D. thesis), Hydraulics & Coastal Engineering Laboratory, Department of Civil Engineering, Aalborg University, Denmark, 2002.

[28] Zahra Shahroozi, Malin Göteman, Jens Engström, Experimental investigation of a point-absorber wave energy converter response in different wave-type representations of extreme sea states, Ocean Eng. 248 (2022) 110693.

[29] Zahra Shahroozi, Malin Göteman, Erik Nilsson, Jens Engström, Environmental design load for the line force of a point-absorber wave energy converter, Appl. Ocean Res. 128 (2022) 103305.

[30] Linus Wrang, Eirini Katsidoniotaki, Erik Nilsson, Anna Rutgersson, Jesper Rydén, Malin Göteman, Comparative analysis of environmental contour approaches to estimating extreme waves for offshore installations for the baltic sea and the north sea, J. Mar. Sci. Eng. 9 (1) (2021) 96.

[31] Eirini Katsidoniotaki, Erik Nilsson, Anna Rutgersson, Jens Engström, Malin Göteman, Response of point-absorbing wave energy conversion system in 50-years return period extreme focused waves, J. Mar. Sci. Eng. 9 (3) (2021) 345.

[32] Zahra Shahroozi, Malin Göteman, Jens Engström, Experimental results of force measurements from a scaled point absorbing wave energy converter subjected to extreme waves, in: Proceedings of the Fourteenth European Wave and Tidal Energy Conference, EWTEC, 2021.

[33] François Chollet, et al., Keras, 2015, https://github.com/fchollet/keras.

[34] Martín Abadi, et al., TensorFlow: Large-scale machine learning on heterogeneous systems, 2015, URL https://www.tensorflow.org/, Software available from tensorflow.org.

[35] Zahra Shahroozi, Malin Göteman, Jens Engström, A neural network approach to minimize line forces in the survivability of the point-absorber wave energy converters, in: Proceedings of the 42nd Ocean, Offshore and Arctic Engineering Conference, OMAE 2023, 2023, in press.

[36] Uppsala University UPPMAX, Rackham cluster, 2024, URL https://www.uppmax.uu.se/resources/systems/the-rackham-cluster. (Accessed 1 May 2024).

[37] Alexandra Anne Elizabeth Price, David IM Forehand, A Robin Wallace, Time-span of future information necessary for theoretical acausal optimal control of wave energy converters, in: 2009 European Control Conference, ECC, IEEE, 2009, pp. 3761–3766.

[38] DNV, Recommended practice DNV-RP-C205: environmental conditions and environmental loads, DNV, Norway (2010).

[39] Dezhi Ning, Boyin Ding, Modelling and Optimization of Wave Energy Converters, CRC Press, 2022.

[40] Jørgen Hals, Modelling and phase control of wave-energy converters, 2010.

[41] Gene F Franklin, J David Powell, Michael L Workman, et al., Digital Control of Dynamic Systems, vol. 3, Addison-wesley Menlo Park, CA, 1998.
[42] Michael J. Grimble, Robust Industrial Control: Optimal Design Approach for Polynomial Systems, Prentice-Hall, Inc., 1994.
[43] Edoardo Pasta, Nicolás Faedo, Giuliana Mattiazzo, John V Ringwood, Towards data-driven and data-based control of wave energy systems: Classification, overview, and critical assessment, Renew. Sustain. Energy Rev. 188 (2023) 113877.
[44] Zhong-Sheng Hou, Zhuo Wang, From model-based control to data-driven control: Survey, classification and perspective, Inform. Sci. 235 (2013) 3–35.
[45] Lucian Buşoniu, Tim De Bruin, Domagoj Tolić, Jens Kober, Ivana Palunko, Reinforcement learning for control: Performance, stability, and deep approximators, Annu. Rev. Control 46 (2018) 8–28.
[46] Lukas Hewing, Kim P Wabersich, Marcel Menner, Melanie N Zeilinger, Learning-based model predictive control: Toward safe learning in control, Annu. Rev. Control Robotics Auton. Syst. 3 (2020) 269–296.
[47] Kenneth J Hunt, D Sbarbaro, R Żbikowski, Peter J Gawthrop, Neural networks for control systems—a survey, Automatica 28 (6) (1992) 1083–1112.

Further reading

[1] Zahra Shahroozi, Malin Göteman, Jens Engström, Jørgen Hals Todalshaug, Considerations on prediction horizon and dissipative losses for wave energy converters, IET Renew. Power Gener. 15 (14) (2021) 3434–3458.